Materials & Design 232 (2023) 112147

Contents lists available at ScienceDirect

Materials & Design

journal homepage: www.elsevier.com/locate/matdes

Multi-scale model to simulate stress directionality in laser powder bed fusion: Application to thin-wall part failure

Reza Tangestani [a], Apratim Chakraborty [a], Trevor Sabiston [a], Lang Yuan [b], Morteza Ghasri-Khouzani [a], Étienne Martin [a,c,*]

[a] University of Waterloo, 200 University Avenue West, Waterloo, ON N2L 3G1, Canada
[b] University of South Carolina, 301 Main Street, Columbia, SC 29208, United States
[c] Polytechnique Montréal, 2500 Chemin de Polytechnique, Montréal, QC H3T 1J4, Canada

ARTICLE INFO

Keywords:
Laser powder bed fusion
Superalloys
Additive manufacturing
Failure
Numerical modelling
Thin-wall

ABSTRACT

In this study, line heat inputs are lumped to improve the computational efficiency while preserving stress directionality in laser powder bed fusion (LPBF). The lumped hybrid line (LHL) model predicts part distortion accurately within 10 μm of the experimental error in reasonable time. The effects of part geometry and scanning strategies on part distortion and failure during LPBF of thin-wall components are evaluated. Eight different printing patterns including different vector lengths and interlayer scan rotations for five different part lengths are studied. Simulation results show that the compressive stresses in the longitudinal and build directions create buckling, which limits subsequent layer deposition. This causes in-process part failure called the limiting build height (LBH) effect. A strong correlation between the vector length and residual stresses is shown. Longer vector lengths generate smaller compressive residual stresses along the build direction while inter-layer scan rotations homogenize the internal stresses in the scanning plane. Increasing the vector length and introducing scan rotations are useful processing strategies to improve the LBH. Moreover, part failure can be mitigated by varying the part geometry. Increasing the part thickness reduces the susceptibility to buckling and increases the LBH, whereas part length alters the failure mode.

1. Introduction

Superalloys are excellent materials for application in aerospace and power industries due to superior mechanical properties at elevated temperatures [1–5]. Turbine blades and fuel nozzles are examples of complex structures commonly used in these industries [6,7]. Additive manufacturing (AM) processes such as binder jet [8–10] and laser powder bed fusion (LPBF) [11] offer near-net-shape fabrication of such features. The LPBF technology has several advantages such as high density [12], good mechanical strength [13], and high dimensional accuracy [14]. However, build defects such as surface roughness [15], micro-cracking [16], and part distortion [17,18] diminish the final part quality.

Thin-wall part fabrication using LPBF is especially challenging. One reason for this challenge is in-process part failure, which occurs when the final built height of the thin-wall component is lower than the initial designed height. The limiting build height (LBH) terminology was introduced in [17] to describe this phenomenon. The LBH, defined as the maximum achievable height for the component, is affected by the residual stress, distortion, and buckling. The created residual stresses cause buckling and generate excessive part deformation leaving empty space for the new layer to be deposited. Several parameters affect the residual stresses during LPBF [19]. For instance, printing patterns and vector length affect the stress state in LPBF thin-wall parts. Tangestani et al. [20] utilized a thermomechanical numerical simulation to predict residual stresses during the LPBF process. The authors showed that printing patterns are more significant than laser power on the residual stresses. However, very small thin-wall parts (3 mm^3) were evaluated in this study due to model speed limitation. Part geometry also affects the processability of thin-wall parts using LPBF. Chakraborty et al. [17] studied the effect of part thickness on LBH using experimental and numerical simulation methods. The authors showed that thinner parts are more susceptible to part distortion, buckling, and premature part failure during LPBF. However, only three part thicknesses were studied and the effects of other part dimensions on in-process stresses and LBH were not investigated.

Finite element modelling (FEM) is a cost-effective method to

* Corresponding author.
E-mail address: etienne.martin@polymtl.ca (É. Martin).

https://doi.org/10.1016/j.matdes.2023.112147
Received 26 March 2023; Received in revised form 28 June 2023; Accepted 6 July 2023
Available online 16 July 2023
0264-1275/© 2023 The Authors. Published by Elsevier Ltd. This is an open access article under the CC BY-NC-ND license (http://creativecommons.org/licenses/by-nc-nd/4.0/).

Nomenclature

Acronym	Description
LPBF	laser powder bed fusion
LBH	limiting build height
FEM	finite element modelling
HL	hybrid line
ED	exponential decaying
LH	layer heating
LHL	lumped hybrid line
R108	RENÉ 108
DOE	design of experiment
VL	vector length
ES	extra-short printing pattern
EL	extra-long printing pattern
S	short printing pattern
L	long printing pattern
ES-EL	extra-short-extra-long printing pattern
S-S	short-short printing pattern
L-L	long-long printing pattern
R	random printing pattern
EDM	electrical discharge machining
CAD	computer aided design
CPU	central processing unit

evaluate the effect of processing parameters on part integrity. Many researchers suggest the layer (flash) heating technique for part-scale simulation and residual stress prediction [21,22]. This approach uses uniform heat application over the layer, with one or more layers simulated in each step. Layer heating eliminates the effect of printing pattern on stress directionality, essential to study the buckling phenomenon.

To resolve the induced stress anisotropy, the laser movement must be modelled at the laser beam scale [23]. High-fidelity thermal stress models are useful to accurately simulate the complex in-process stresses and strains by considering the inherently complex melt pool physics and temperature gradients developed during the AM process [24,25]. Chen et al., [24] used a computational fluid dynamics (CFD) model coupled with the quiet element method (QEM) in a FEM mechanical model to account for the complex melt pool geometry, melting/remelting, solidification, and molten pool flow effects during the AM process. The authors predicted the stresses, strains, and defects (such as voids and cracks) accurately with respect to the experimentally processed single tracks. Similarly, Hu et al. [25] used combined thermal-fluid flow, phase field, and crystal plasticity FEM models to accurately determine the residual stresses developed at the grain-scale with respect to the laser scanning direction. However, both the high-fidelity thermal stress and beam-scale models are computationally expensive for part-scale simulations [24,26].

The line heat input model is a beneficial approach to enhance the simulation time [27]. Tangestani et al. [20] used the line heating method to simulate the effect of laser scanning strategy on LPBF processing of thin-wall parts. The authors developed a hybrid line (HL) heat input model with the exponential decaying (ED) heat source to simulate 5 × 0.5 × 1.2 mm (length × thickness × height) components within 63 h. The authors showed that using the HL model could increase the simulation time over 150 times compared to the ED heat input model. However, the model size is too small to simulate the actual in-process part failure causing LBH. Lumping line heat inputs and layers reduces the processing time [28]. Bayat et al. [29] conducted a parametric study on the impact of lumped track and layer numbers on model resolution. The simulated component was 30 × 1 × 30 mm and only took around 40 h to solve. A parametric study on the impact of lumped track and layer numbers on model resolution was conducted. The authors reported a strong correlation between lumped layers, tracks, and deformation prediction accuracy, proposing fewer (2–75) lumped tracks improve the model accuracy. However, the model simulates tracks with only one increment, neglecting the effect of laser movement along the laser track. Luo et al. [30] showed the importance of laser track segmentation on the simulation of anisotropic stress distribution in thin-wall parts. The authors used smaller segmentation at the corners and larger segmentation at the centre of the part to maintain accuracy and enhance computational efficiency.

In this study, a new multi-scale FEM model is developed to simulate the LPBF process and capture stresses at the track and part scales in a single simulation. The lumped HL (LHL) and layer heating (LH) modelling techniques are combined offering improved computational efficiency and preserving the stress directionality. The model is validated using a large design of experiment consisting of thirty-five parts with different part lengths, printing patterns, and inter-layer scan rotations. The effects of part geometry and laser scan strategy on premature LPBF thin-wall part failure are investigated. The underlying LBH mechanisms and optimal printing parameters for part failure mitigation are determined.

2. Material and experimental methods

2.1. Feedstock material

The high-γ' Ni-based superalloy RENÉ 108 (R108) powder was used as feedstock for the LPBF process. Gas-atomized powder, mainly spherical with an average size of 19 μm (D_{50}) and a size distribution of 12–40 μm (D_{10}-D_{90}), was provided by Powder Alloy Corporation (PAC). The chemical composition was 8.64 Cr, 10 Co, 10.03 W, 0.53 Mo, 0.75 Ti, 5.36 Al, 0.87 Hf, 0.01 Zr, 0.01C, 3.02 Ta, 0.01B and balance Ni (in wt. %). The alloy contained 6.11 wt% Al + Ti and 63% γ' volume fraction [31], identified as a hard-to-weld material in literature [32,33]. The material poses challenges for 3D printing applications due to in-process failures and micro-cracks in the as-built parts.

2.2. LPBF process

An Aconity MIDI LPBF machine was used to print 35 thin-wall parts under an argon environment. The laser speed was set to 1000 mm/s, power 200 W, layer thickness 40 μm, laser radius 60 μm, and hatch spacing 90 μm. These process parameters were identical for all the fabricated parts. Fig. 1 illustrates the design of experiment (DOE) and orientation of the printed parts with respect to the build plate. The components were placed at an angle of 75°with respect to the recoater travel direction, as shown in Fig. 1a. The distance between individual and groups of parts was set to 5 mm and 10 mm, respectively. All parts were set to 0.5 mm thickness and 30 mm height, as shown in Fig. 1b.

The DOE was constructed to evaluate the influence of part length and scanning strategy on the LBH and part distortion. Four different part lengths (30 mm, 40 mm, 50 mm, and 60 mm) were studied, as illustrated with different colors in Fig. 1a. Each part is labeled (1, 2, 3, 4, 5, etc.,) according to its printing pattern.

Eight different printing patterns (numbered 1 to 8) with different vector length combinations were considered, as detailed in Table 1. The vector length was modified by changing the laser scan (vector) angle for each layer. A schematic showing the vector angle ($\theta_{v,n}$, where n is the layer number) with respect to the scanning plane is presented in Fig. 2a. The vector angle is defined as the angle of a single laser scan with respect to the part length (X-direction) on a given layer. Printing patterns include scans with or without rotation between successive layers, indicated using the parameter θ_R describing the inter-layer scan rotation

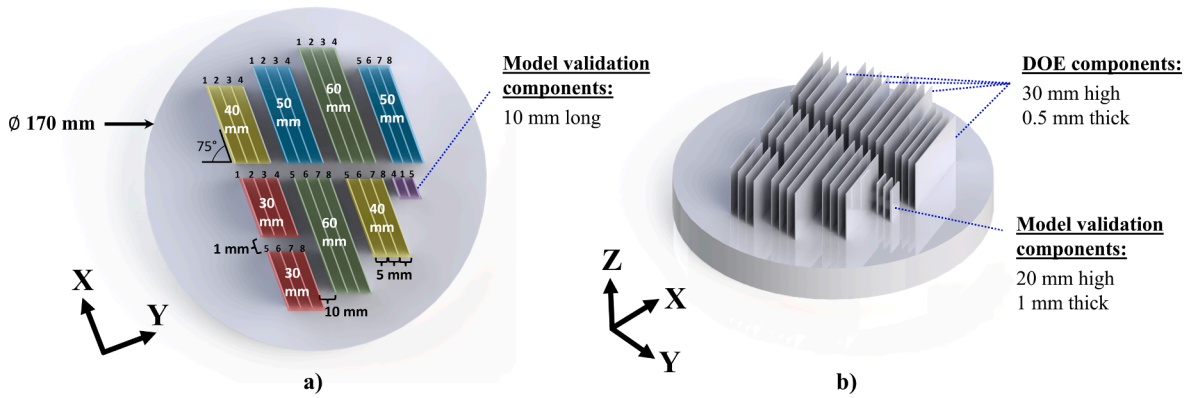

Fig. 1. The DOE and configuration of thin-wall components on the build plate shown in a) top 2D and b) 3D views. All components, except the three used for validation, have identical thicknesses and heights, but varying lengths and printing patterns. Parts with identical lengths are grouped and labelled using color codes. Annotations are added to describe printing patterns (1, 2, 3, etc.,) detailed in Table 1.

Table 1
The printing patterns used to manufacture the thin-wall components. The vector angles for the first 5 and nth layers are included under the column group labelled "Vector Angle (°) for Each Layer". Each printing pattern corresponds to the label presented under the "Name" column. Printing patterns 5–8 include scan rotations between layers.

Printing Pattern Label	Name	Vector Angle (°) for Each Layer					
		1	2	3	4	5	n
1	Extra-short (ES)	90	90	90	90	90	90
2	Small (S)	75	75	75	75	75	75
3	Long (L)	15	15	15	15	15	15
4	Extra-long (EL)	0	0	0	0	0	0
5	ES-EL	90	0	90	0	90	0,90
6	S-S	75	105	75	105	75	75,105
7	L-L	15	165	15	165	15	15,165
8	R	67	134	201	268	335	67 × n

angle (see Fig. 2b). By varying $\theta_{v,1}$ and θ_R, a wide range of vector lengths is covered. Layer-wise implementations of the 8 printing patterns (detailed in Table 1) are illustrated for the first four part layers, as shown in Fig. 2c. For instance, when $\theta_{v,1} = 90^\circ$ and $\theta_R = 0^\circ$, a scanning pattern with the shortest vector length (called extra-short ("ES")) is created. Alternatively, when $\theta_{v,1} = 90^\circ$ and $\theta_R = 0^\circ$, a scanning pattern with the longest vector length (called extra-long ("EL")) is produced. Intermediate vector angles of 15° and 75° generate printing patterns with short ("S") and long ("L") vector lengths, respectively. In all cases above, $\theta_{v,n}$ remains constant for all build layers since no inter-layer scan rotation ($\theta_R = 0^\circ$) is used.

When inter-layer scan rotation is applied ($\theta_R \neq 0^\circ$), the printing patterns show different vector angles for each layer, as listed in Table 1 and illustrated in Fig. 2c. A 90° inter-layer scan rotation ($\theta_R = 90^\circ$) applied to the "EL" printing pattern generates alternating shortest and longest vector lengths, called extra-short-extra-long ("ES-EL"). Alternating 150° inter-layer scan rotations ($\theta_R = \pm 150^\circ$) applied to the "S" and "L" printing patterns generates short-short ("S-S") and long-long ("L-L") printing patterns, respectively. A continuous 67° scan rotation ($\theta_R = +67^\circ$) between layers produces the random ("R") printing pattern including varying short and long vector lengths in subsequent layers along the part height.

For model validation purposes, three additional components with identical dimensions of 10 × 1 × 20 mm (length-X × thickness-Y × height-Z) were fabricated using the "EL", "ES", and "ES-EL" printing patterns. These printing patterns exhibited the largest stress discrepancy in a previous study [20]. The part thickness was maximized to achieve the design height and enable experimental measurements of the deformed shape.

2.3. Evaluating printed part deformations

Accurate measurement of residual stresses in the additively manufactured component is costly and time-consuming [34]. In this study, the model was validated by measuring the part deformation using a SmartScan 3D scanner provided by AICON. The scanner is capable of measuring deformations with a precision of 10 μm with its S – 150 mm lens [35]. Thicker components (1 mm) were added to the DOE for model validation because the scanner cannot accurately measure the shape of thinner parts. The printed parts were extracted from the build plate using wire electrical discharge machining (EDM). The build plate was kept noticeably larger than the printed parts to prevent part distortion during removal. The final 3D-scanned geometry was constructed by merging 30 individual 3D scans acquired at 12° increments. To verify the simulation results, the measured and predicted distortions were compared. The measured deformation with respect to the designed CAD component was visualized using the PolyWorks software.

2.4. Limiting build height measurement

The limiting build height (LBH) is defined as the distance between the build plate and the built part position showing the first sign of partial or complete failure, as demonstrated in Fig. 3. Partial LBH failure is considered for components showing preliminary signs of part failure, as shown in Fig. 3a. Complete LBH failure is considered for parts with clean failure at the summit, as shown in Fig. 3b. A digital caliper was used to measure the LBH values of all as-printed parts attached to the build plate. Further details on the part failure mechanisms causing the observed LBH effects are provided in section 5.2.

3. Modeling

Dassault System's finite element software, Abaqus, was used to model the LPBF process. A detailed description of the AM model, including its ability to predict stress and deformation during and after the process, is provided in this section. The in-process results provide insights into the contribution of part geometry and printing pattern to the final part distortion and LBH.

3.1. Simulation of LPBF process

A sequentially coupled FEM model including thermal and mechanical simulations was used to simulate the LPBF process. Firstly, a thermal model was developed to calculate the nodal temperature (temperature

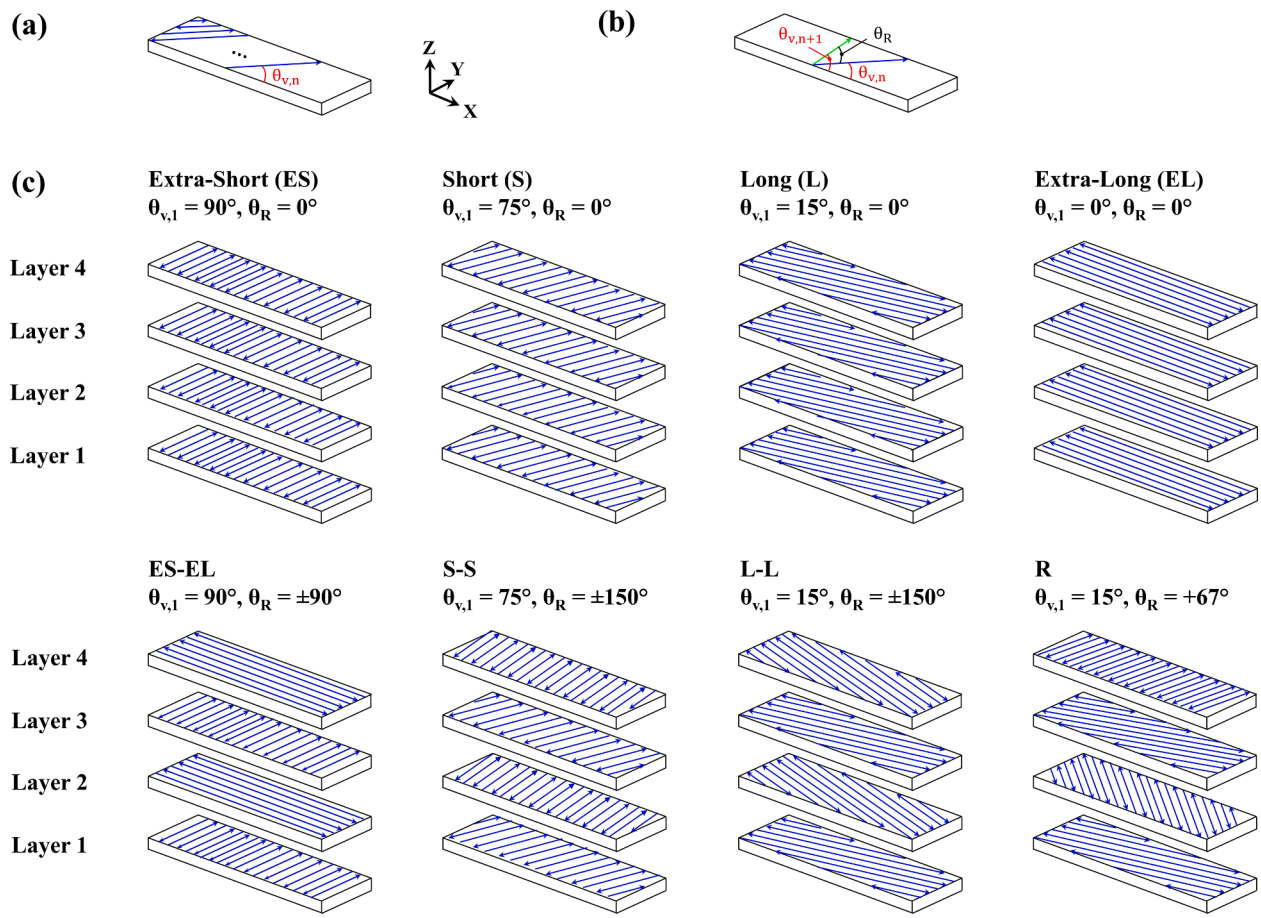

Fig. 2. Schematics showing (a) nth layer scanning angle ($\theta_{v,n}$) with respect to the part length (X-axis), (b) scan rotation angle (θ_R) between layers n and n + 1, and (c) printing patterns (combinations of $\theta_{v,1}$ and θ_R) employed in this study. Scan vector variations between layers 1–4 are shown for each printing pattern using blue arrows representing vectors. For further details, refer to Table 1. (For interpretation of the references to color in this figure legend, the reader is referred to the web version of this article.)

Fig. 3. LBH measurement criteria for a) partial and b) complete part failure. The red lines indicate the end positions of the LBH measurements. (For interpretation of the references to color in this figure legend, the reader is referred to the web version of this article.)

value associated with each node of an element) using the traditional heat transfer equation Eq. (1):

$$\rho C_p \frac{\partial T}{\partial t} = \frac{\partial}{\partial x}\left(k\frac{\partial T}{\partial x}\right) + \frac{\partial}{\partial y}\left(k\frac{\partial T}{\partial y}\right) + \frac{\partial}{\partial z}\left(k\frac{\partial T}{\partial z}\right) + Q_{\forall} \tag{1}$$

where ρ is density (8027 kg/mm^3 [36]), C_p is specific heat capacity (temperature-dependent taken from [36,37]), T is nodal temperature, k is thermal conductivity (temperature-dependent taken from [36]), and $Q_{\forall}$ is laser heat input. The heat loss from the open surfaces was simulated for conductive, convective, and radiative heat transfer using Eq. (2):

$$\overbrace{k\frac{\partial T}{\partial x}}^{Conduction} = \overbrace{h(T - T_\infty)}^{Convection} + \overbrace{\varepsilon\sigma_{SB}(T^4 - T_\infty^4)}^{Radiation} \tag{2}$$

where h is the convection coefficient set at 20 $\left(\frac{W}{m^{2o}C}\right)$, as recommended for superalloy thin-wall parts with wall thicknesses smaller than 1 mm [38], ε is the emissivity set at 0.4 (as done in the previous study [20]), and σ_{SB} is the Stephan-Boltzmann constant (5.67 × 10^{-8} W/m^{2}K). The nodal temperatures were computed by solving the derivative Eq. (1) and using Eq. (2) as boundary conditions (heat loss equation). Next, a mechanical model was used to calculate the incremental strain $\Delta\varepsilon_{ij}^T$ due to thermal expansion, as shown in Eq. (3):

$$\Delta\varepsilon_{ij}^T = \alpha\Delta T\delta_{ij} \tag{3}$$

where α is the thermal expansion coefficient (taken from [36]), ΔT is the incremental temperature rise and δ_{ij} is the Kronecker delta function ($\delta_{ij} = 1 if i = j, \delta_{ij} = 0 if i \neq j$). The total strain increment $\Delta\varepsilon_{ij}$ acting in the

material was calculated using Eq. (4):

$$\Delta\varepsilon_{ij} = \Delta\varepsilon_{ij}^{E+P} + \Delta\varepsilon_{ij}^{T} + \Delta\varepsilon_{ij}^{\Delta V} + \Delta\varepsilon_{ij}^{Trp} \tag{4}$$

where $\Delta\varepsilon_{ij}^{E+P}$ is the combination of the elastic and plastic strain, $\Delta\varepsilon_{ij}^{\Delta V}$ is the volumetric strain resulting from phase transformation, and $\Delta\varepsilon_{ij}^{Trp}$ is the transformation plasticity. In this study, the volumetric and transformation strains were assumed to have negligible effect on the total strain and set to zero [19,29]. For elastic deformation, Eq. (5) was used to predict the stress:

$$\Delta\sigma_{ij}^{mech} = D_{ijlm}.\Delta\varepsilon_{lm}^{E} \tag{5}$$

where D_{ijlm} is the fourth order isotropic elastic stiffness tensor calculated from Young's modulus (E) and Poisson's ratio (v), both taken from [9,39]. D_{ijlm} is given by Eq. (6):

$$D_{ijlm} = \frac{E}{1+v}\left[\frac{1}{2}\left(\delta_{ij}\delta_{lm} + \delta_{il}\delta_{jm}\right)\frac{v}{1-2v}\delta_{ij}\delta_{lm}\right] \tag{6}$$

The convex cutting plane algorithm was used to calculate stresses in the plastic region by enforcing the von Mises yield criterion and using isotropic hardening [40]. The algorithm is used by the FEA software to calculate plastic deformations iteratively using the yield function f (Eq. (7), plastic strain ε_p (Eq. (8) and flow vector a (Eq. (9), as shown:

$$f = \sigma_m - \sigma_y(\varepsilon_q, T) \leq 0 \tag{7}$$

$$\dot{\varepsilon_p} = \dot{\varepsilon_q} a \tag{8}$$

$$a = \left(\frac{\partial f}{\partial \sigma}\right)^T \tag{9}$$

where σ_m is the Mises stress, σ_y is the yield stress [9,39], and ε_q is equivalent plastic strain.

3.1.1. The AM FEM model

A Python script was written to automate the simulation of a large number of components to speed model setup and run times. The framework presented in Fig. 4 allows sequentially coupled thermal and mechanical models to run almost simultaneously. In the simulation workflow, each mechanical model is executed immediately after the completion of the corresponding thermal model in a sequential manner. This approach ensures that the thermal results from one layer are utilized as input for the subsequent mechanical analysis. The inputs include printing patterns (in LSR format) generated from AUTOCAD Netfabb and machine settings (such as laser power and speed). The Python script used these inputs to generate the geometry, mesh, and boundary conditions. Isotropic temperature-dependent R108 material properties were taken from [9,36,37,39,41], based on dendrite growth directions of directionally solidified superalloys. The simulation started with the base plate fixed from displacement in all directions at an initial temperature of 25 °C.

The Abaqus "*Model Change" feature was used to simulate the material deposition, then heat was applied to the layer to replicate the heating process [42,43]. A ten-second cooling period was included on completion of each layer scan to replicate the recoater action during the LPBF process. The simulated geometries are classified into the following three categories:

Three components for validation: In order to verify the accuracy of the simulation, the model validation component was simulated, as shown in Fig. 1.

The simulated components from the DOE: Simulations of all 35 experimental components were performed to study the effects of part length and printing pattern on generated residual stresses.

Two thick components from literature: The effect of wall thickness on residual stress and LBH was examined using two components with identical sizes of 50 × 50 × 1 mm and scanned using the "ES" and "EL" printing patterns.

3.1.2. The heat source model

Simulation of the entire LPBF process at the beam scale is computationally expensive due to the small laser size and layer thickness. In typical beam-scale AM simulations, there are over one million time steps and elements making this heat input inefficient for part scale simulations

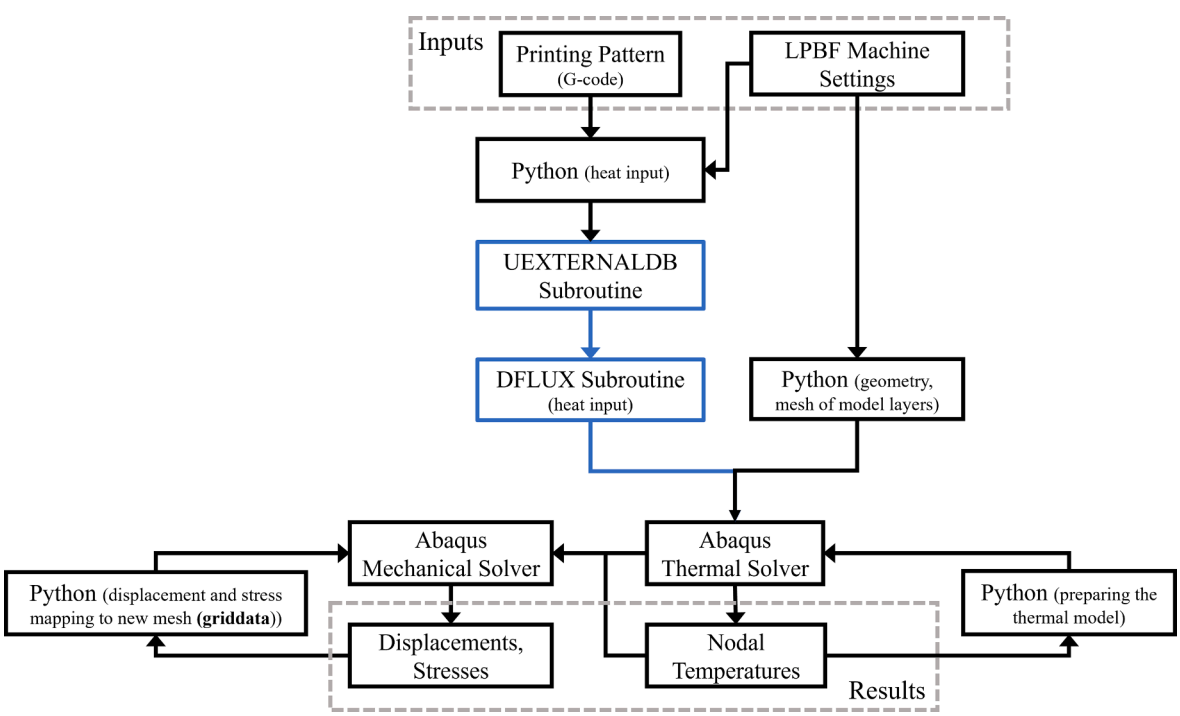

Fig. 4. Flowchart of the computational framework including subroutines (blue) and interactions with customized Python programs. (For interpretation of the references to color in this figure legend, the reader is referred to the web version of this article.)

[27]. Researchers overcome this problem by simulating the laser process with a much larger heat input than the actual laser size. Commonly used methods to model the heat input include the lumped heat input and layer heating (flash heating) techniques. This study utilizes a multi-scale modelling technique combining the lumped HL (LHL) and layer heating (LH) heat input models to enhance the computational efficiency while maintaining accuracy for LPBF process simulations at track and part scales. Each heat input is explained as follows:

I. Lumped hybrid line (LHL) models

The small beam diameter limits the step time and increases the processing time. To overcome this problem and allow resolution of stresses at the track scale [20], the hybrid line (HL) [44] heat input model (Fig. 5a) was applied. The HL model, parameterized using the time step (as shown in Eq. (10), is beneficial to decrease the number of step times.

$$Q=\frac{P\eta}{\sqrt{2\pi}\Delta t v H r_l}e^{\left(-\left|\frac{z}{H}\right|-2\left(\frac{y}{r_l}\right)^2\right)}\left(\mathrm{erf}\left(\frac{\sqrt{2}(x_{end}-x)}{r_l}\right)-\mathrm{erf}\left(\frac{\sqrt{2}(x_{start}-x)}{r_l}\right)\right) \tag{10}$$

where P is the laser power (200 W) and η is the absorption factor (0.5 [44]). The function erf is the error function, while x_{start} and x_{end} are the spatial start and endpoints of the heat input model. These two variables are defined by the beam radius (r_l – 60 μm), laser speed (v – 1000 mm/s) and time step (Δt). For ease of reference, the normalized value of τ, which is the ratio of the laser travel ($v\Delta t$) over the beam radius, was used following Eq. (11):

$$\tau=\frac{v\Delta t}{r_l} \tag{11}$$

For the "EL" printing pattern, the maximum value of τ was set to 60 due to wall thickness limitation similar to [44]. This value was optimized for the EL scanning strategy and 30 mm long-0.5 mm thick parts.

Part manufacturing using LPBF typically involves printing thousands of tracks. To reduce the computational time, layers and tracks are grouped together using the lumping technique. Lumping the HL models yields substantial reduction in the computational time, essential to efficiently simulate stresses at the part scale. Herein, the lumped HL approach is referred to as LHL, illustrated using Fig. 5b-d. Fig. 5b and c show schematic representations of HL layer and track lumping of two laser lines, respectively. Fig. 5d illustrates a lumped HL (LHL) heat input with 3 layers consisting of 3 tracks each. This reduces the computational time by 9X compared to a single laser line (Fig. 5a). According to Bayat et al. [29] and An et al. [21], lumping up to 20 layers with 20 tracks each produces accurate results. In this study, up to 10 layers with 2 to 16 tracks each were lumped to ensure the model's accuracy. The number of lumped sets was determined by the total number of tracks within a layer, which depends on the printing pattern. For example, 16 tracks were lumped for ES and 2 tracks were lumped for the EL printing patterns. These numbers ensure to keep a minimum number of 3 tracks per layer, based on [29]. This allows to maintain reasonable accuracy of the predicted residual stress and computational efficiency.

Implementation in ABAQUS required the UEXTERNALDB subroutine (shown in Fig. 4) that handled reading text files with multiple CPUs. It read the data only at the start of each increment, reducing the frequency compared to reading at every iteration and integration point. The text file was in LSR format and contained laser location information throughout the simulation time. More details and in-depth analysis are available in a previous study [20].

Next, the data obtained from UEXTERNALDB was sent to DFLUX subroutine to compute the heat input magnitude on the material (see blue boxes in Fig. 4). The calculated heat input was sent to the solver to predict the temperature, strain, and stress for the designated increment. The cyclic repetition of this process alongside the mesh coarsening algorithm (explained in section 3.1.3) generated the in-process data for the whole process.

II. Layer heating (LH) model

It is common practice to activate and heat an entire layer at once (see Fig. 5e) to simulate the addition of a layer in a single time step [45,46]. In order to further reduce computation time, layers can be grouped together and simulated at one time. This technique is called the layer heating (LH) approach and the volumetric heat input is given by Eq. (12):

$$Q=\frac{P\eta}{w\times H\times D} \tag{12}$$

where w is the melt pool width (135 μm [44]), H is the lumped layer thickness, and D is the beam diameter (120 μm). To maintain the model accuracy and decrease the processing time, only the first 50 layers (5 lumped layers) were simulated using the LH model in [47], which does not affect the simulation results.

3.1.3. Meshing algorithm

Coarser element sizes help to speed up computations and finer elements are necessary to capture deformation in materials with inhomogeneous temperature fields and high nodal temperatures. The element sizes are smaller for the top layers due to interaction with the laser, but they are more flexible for the outer layers because of lower nodal temperature and more uniformity. During the process, layers may become more distant from the top layer and can be modelled with coarser elements. This highlights the importance of using dynamic meshes to increase the element size as the simulation progresses and reduces the

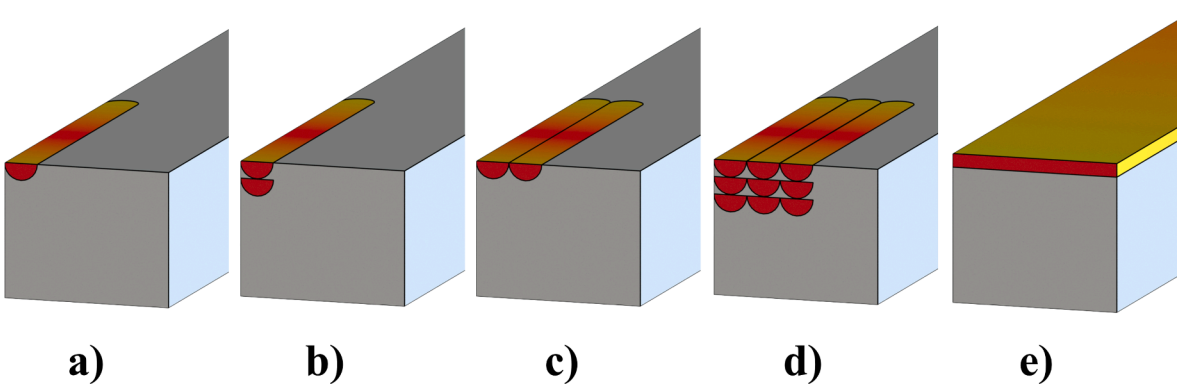

Fig. 5. Set of schematics showing a) single HL, b) HL layer lumping, c) HL track lumping, d) HL three-layer-three-track lumping, e) layer heating (LH) modelling techniques. Note that b-d illustrate lumped HL (LHL) heat inputs.

computation time while maintaining the model accuracy.

A Python code was developed to perform dynamic mesh coarsening with the Abaqus "mesh-to-mesh solution mapping" feature [48,49]. This enables mapping of the nodal temperature (for the thermal model) and stress, plastic strain (for the mechanical model) from older (finer) to newer (coarser) meshes in a systematic manner as the build progresses. Dynamic meshing was applied to groups of layers activated at once to enhance computational efficiency. Detailed schematics and explanations on this subject are provided in [20]. Initially, when the first few layers were built on the substrate, fine mesh sizes (200 × 100 × 80 μm) were utilized. However, as new layers were added, the mesh sizes of the first few layers were dynamically increased (300 × 150 × 160 μm) and mapping from the older fine mesh to the new coarsened mesh was performed through linear interpolation. This process was repeated up to the last layers and the final mesh distribution is shown in Fig. 6.

To ensure model accuracy, more conservative mesh sizes and coarsening rates relative to [48] were adopted for groups of layers (illustrated with different colors in Fig. 6) with identical mesh sizes. The TIE feature in ABAQUS was used to establish and maintain complete connectivity between adjacent mesh groups. This ensures connectivity and accounts for traction effects between finer and coarser mesh sizes [48]. Meshes for the thermal and mechanical models consisted of DC3D8 and C3D8 element types, respectively, and the element sizes employed for each mesh group are provided in Table 2. The element size was gradually increased during the process in accordance with [48]. This avoids abrupt changes and discontinuities in the simulated results [49]. The finest element sizes were used for the first 50 layers to account for the laser interaction, rapid heating, and rapid cooling according to [48]. For layers 51 to 150, the element size was increased in all directions to enhance computational efficiency. For layers 151 to the base of the component, the element size in the Z direction was kept constant to ensure model accuracy based on previous suggestions [20].

4. Model evaluation

4.1. Computational time

Average simulation times for parts with 16 mm height, two thicknesses (0.5 mm and 1 mm), and four different lengths (30 mm, 40 mm, 50 mm, 60 mm) are compared in Fig. 7a using LH + LHL heat input. Only the first 50 layers (12.5% of the entire simulation) were simulated using LH and the rest were simulated using LHL. The error bars represent the variation in processing times for the 8 different printing patterns

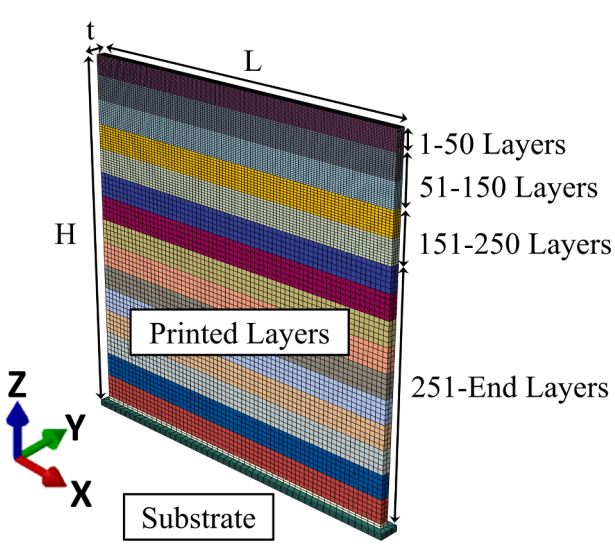

Fig. 6. Part-scale meshed model to simulate the process for different LPBF parameters. Sections are colored to distinguish element sizes in Table 2.

Table 2
Element sizes in microns for each meshed layer of the part-scale simulation.

Layer Number	Length (X), μm	Width (Y), μm	Height (Z), μm
1–50	200	100	80
51–150	300	150	160
151–250	400	200	160
251-End	600	300	160

presented in Table 1. This is because the vector length and the part cross-section dimension affect the number of time steps (τ) required for the HL model.

There is a direct correlation between simulation time and the number of elements, as shown in Fig. 7a. For a given part thickness, increasing the part length increases the number of elements and computational time linearly. More details on the effect of number of elements on simulation time can be found in [50].

The simulation time is also affected by the number of laser tracks required for each printed layer. For example, considering a part length of 30 mm, the average process time increases by 8X when the part thickness increases from 0.5 mm to 1 mm. The LHL lumping parameters are optimized for the 0.5 mm part thickness. The processing time for the 1 mm parts can be reduced by lumping more tracks, but conditions are kept constant here for comparison purposes.

Fig. 7b compares the average processing times for entire part simulations between the layer heating (LH), lumped hybrid line (LHL), and LH + LHL heat inputs (Fig. 7a). Simulation times can be reduced significantly when using only the layer heating (LH) approach. For instance, considering a 60 mm × 0.5 mm × 16 mm (length × thickness × height) part, simulation using LH takes 21 h. However, using the LH heat input alone would eliminate the effect of printing pattern on the residual stress [22], the main topic of this study. The LH + LHL model takes 188 h, 12% faster than using LHL alone (213.7 h).

4.2. Model accuracy

The comparison between printed and simulated part distortion for three different printing patterns ("EL", "ES", "ES-EL" in Table 1) are shown in Fig. 8. All printed parts were 1 mm thick, 10 mm long, and 20 mm high, as described in section 2.2. A MATLAB code was generated to record and plot the predicted deformation.

The predicted and measured deformations are labeled on the components in Fig. 8. All parts demonstrate the same trends. The maximum deformation occurs near the bottom of the part along the wall edge (shown using red boxes). Lower deformation occurs near the middle of the part (blue boxes) and minimum deformation happens at the top of the part (purple boxes). In all cases, the error differential between predicted (Fig. 8a,c,e) and measured (Fig. 8b,d,f) deformation lies within 10 μm.

The largest deformation (132 μm) is situated along the sides of the ES-EL part and the error primarily comes from the front face of the components due to the layer activation approach employed in the model. The "*Model Change" tool activates elements with initial strain from the previous layer, which results in the elimination of small deformations at the surface and smoothens the results. Note that this problem does not significantly affect the residual strain or stress created by large-scale simulations and the technique is commonly used by researchers [29,43]. Therefore, the modeling approach can accurately predict the effect of scanning strategy on part distortion and residual stresses induced by LPBF process.

5. Results

5.1. Experimental observations of LBH in printed thin-wall components

Fig. 9 shows the measured LBH values of the 0.5 mm thick

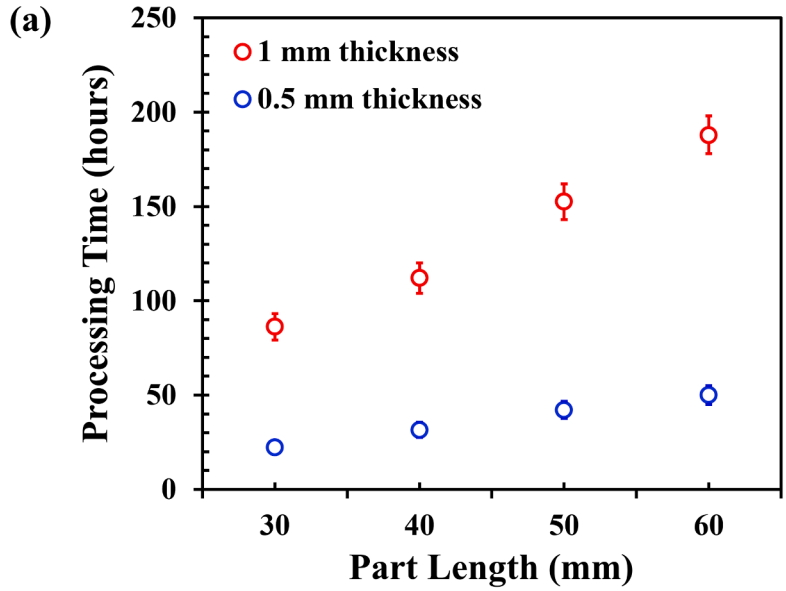

(b)

Part Thickness, Y (mm)	Part Length, X (mm)	Processing Time for Entire Part Simulation (Hours)		
		LH (100%)	LHL (100%)	LH (12.5%) + LHL (87.5%)
0.5	30 mm	5.7	25.1	22.3
	40 mm	7.1	36.2	31.5
	50 mm	8.7	48.1	42.0
	60 mm	10.5	56.5	50
1.0	30 mm	11.0	97.9	86.2
	40 mm	14.0	126.8	112
	50 mm	17.5	173.4	152.5
	60 mm	21.0	213.7	188

Fig. 7. (a) Average processing times to simulate parts with different thicknesses and lengths using the LH + LHL heat input. The part height is kept constant at 16 mm. The error bars show variations between the required times to simulate different printing patterns. (b) Average processing times to simulate 16 mm tall parts with different thicknesses and lengths using the LH, LHL and LH + LHL heat inputs. For the LH + LHL heat input, only the first 50 layers (12.5% of the entire model) were simulated using LH.

components (white, blue, red, and black columns) obtained from the DOE and the 1 mm components (green columns) obtained from [17]. Results include printing patterns without (Fig. 9a) and with inter layer rotations (Fig. 9b). The label above each chart shows the 2 types of failure (labelled (1) and (2)) explained in Section 5.2. The parts with 40 mm length and "S" pattern, 50 mm length and "R" pattern, 50 mm length and "L-L" pattern do not appear in Fig. 9. These components were affected by deviation of the neighboring components and will not be considered in this study.

In Fig. 9, the dashed and full black lines represent the targeted part height for the 0.5 mm and 1 mm thick components, respectively. In total, 6 parts with 0.5 mm wall thickness reached the designed build height (30 mm) and did not exhibit the LBH phenomenon. On the other hand, both 1 mm thick parts demonstrated LBH, not achieving the designed build height (50 mm).

5.1.1. Printing patterns without scanning angle rotations between the layers

A comparison of the scanning strategies in Fig. 9a shows that components with long vector lengths (e.g., "L" and "EL") have greater LBH values than those with short vector lengths (e.g., "S" and "ES"). For example, a 0.5 mm thick component with "S" printing pattern exhibits a LBH between 18 mm and 22 mm (depending on the part length), whereas a part with "L" printing pattern has a LBH between 23 mm and 30 mm. The LBH of a component with 30 mm length increases by 50.3% when the printing pattern changes from "ES" to "EL". For 1 mm thick components, a similar increase in LBH is observed from "ES" to "EL" (~60%), indicating that longer vector length is beneficial to LBH.

5.1.2. Printing patterns with scanning angle rotations between the layers

The LBH values increase when inter-layer scan rotations are introduced, as shown in Fig. 9b. Comparing Fig. 9a and b reveals that "L" and "S" patterns (Fig. 9a) without scan rotations have systematically lower LBH (up to 16%) than their counterparts with inter-layer rotations ("L-L" and "S-S" in Fig. 9b). Increasing the vector length also increases the LBH when inter-layer rotation is incorporated. The "S-S" parts have LBH values ranging between 19 mm and 22 mm, while two of the three "L-L"

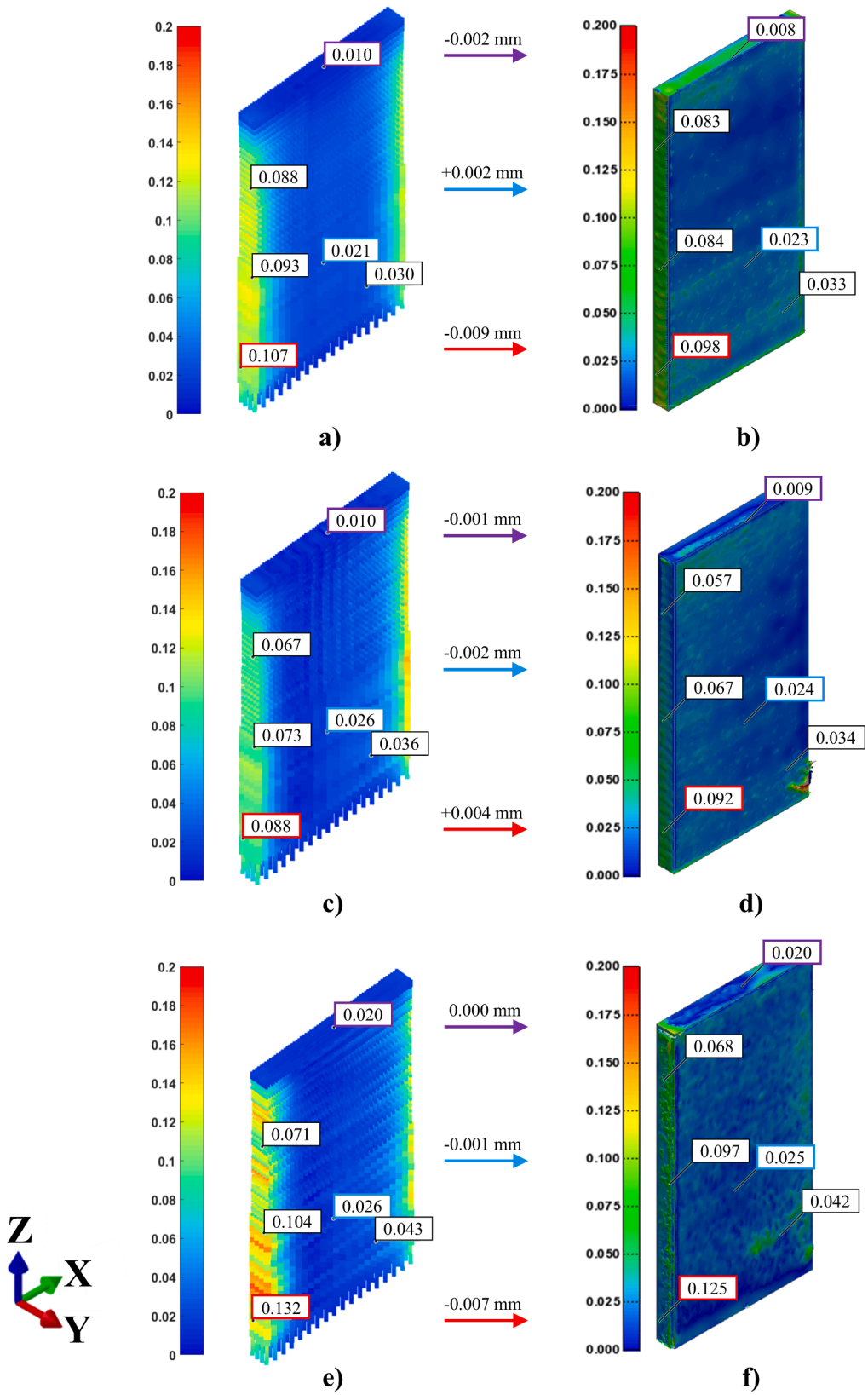

Fig. 8. A comparison between (a), (c), (e) simulation and (b), (d), (f) experimental measurements of part distortion. Three different laser scanning strategies are compared. The deformations (in mm) created by the (a)-(b) "EL", (c)-(d) "ES", and (e)-(f) "ES-EL" scanning strategies are demonstrated. Error differentials between the predicted and measured deformations are shown using red (maximum), blue (medium), and purple (minimum) arrows, corresponding to boxed values with matching color outlines. (For interpretation of the references to color in this figure legend, the reader is referred to the web version of this article.)

parts reach the desired height (30 mm). The LBH values of the continuously rotating printing patterns ("ES-EL" and "R") are similar and lie between the LBH values obtained using the short ("S-S") and long ("L-L") VL patterns. This is because the continuous rotation scans create alternating layers with short and long vectors.

5.1.3. *Effect of part dimensions on thin wall LBH*

Increasing the part length increases the LBH for both rotational and non-rotational printing patterns, as shown in Fig. 9. For example, at a constant wall thickness of 0.5 mm and "ES" printing pattern, doubling the length from 30 mm to 60 mm results in a 20% (4.5 mm)

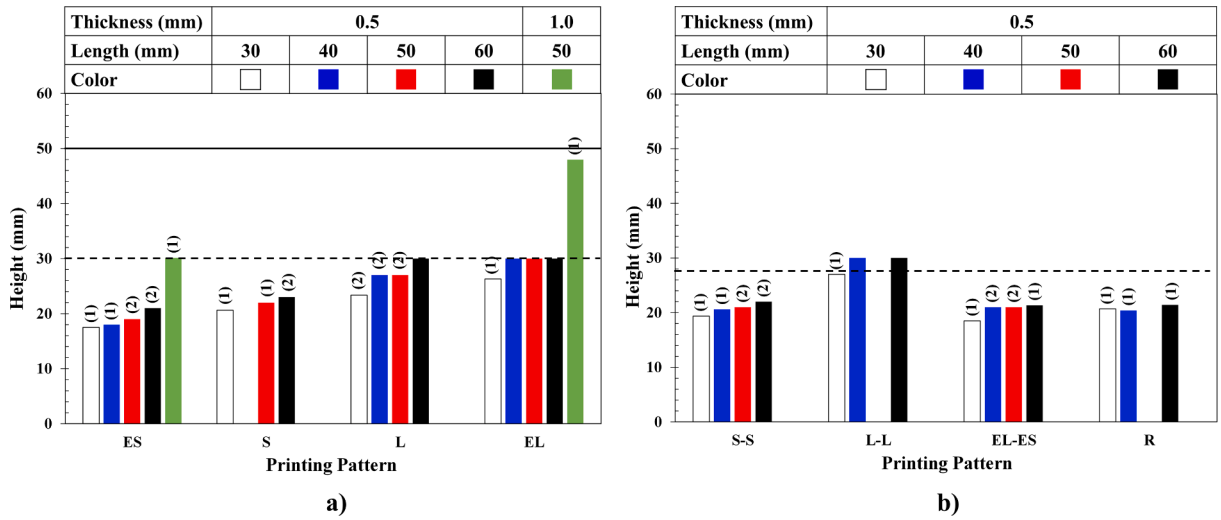

Fig. 9. LBH of the as-built thin-wall parts processed under the conditions described in Table 1. Conditions are split into laser printing patterns a) without and b) with inter-layer scan rotations. Data for the 1 mm thick components (green) are derived from literature [17]. The dotted and full black lines denote the target heights for 0.5 mm and 1 mm part thicknesses, respectively. The column labels correspond to the observed failure mechanisms discussed in section 5.2. (For interpretation of the references to color in this figure legend, the reader is referred to the web version of this article.)

improvement in the LBH. The part length effect is thus significantly smaller than the VL effect on LBH. However, increasing the part thickness generates a more pronounced increase in the LBH. For example, at a constant part length of 30 mm and "ES" printing pattern, the LBH increases by 72% when the wall thickness doubles from 0.5 mm to 1 mm in Fig. 9a. According to [17], thicker parts exhibit higher LBH due to lower susceptibility to buckling during LPBF.

5.2. Part failure mechanisms causing LBH

Two different part failure mechanisms causing LBH are observed in this study, as summarized in Fig. 10. Failure did not initiate from any internal cracking mechanisms as discussed elsewhere [17].

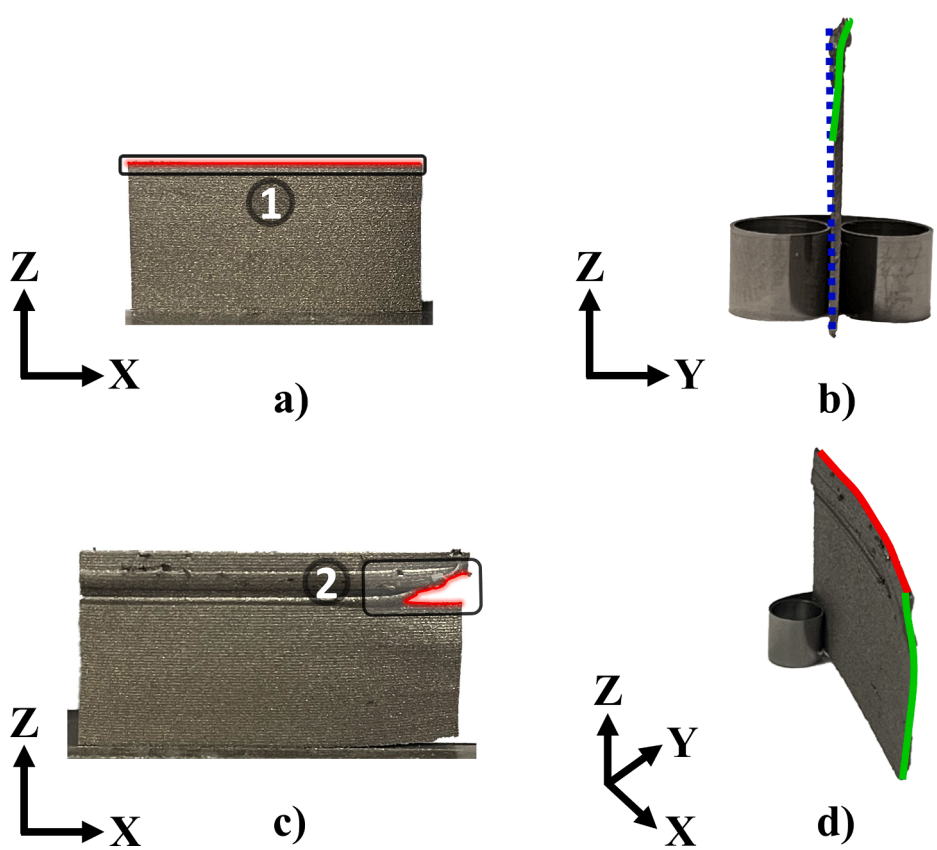

Fig. 10. The two observed failure mechanisms causing LBH during the LPBF process. Mechanism one a) front and b) side views show a clear rupture along the centerline due to buckling in the X-Z plane. Mechanism two c) front and d) side views show failure localized at part corners due to a combination of buckling in the X-Z (rotation about the X axis) and Y-Z planes (rotation about the Z axis).

5.2.1. Failure mechanism one (complete top)

The component is completely detached at the top layer as shown in Fig. 10a. A similar type of failure was previously reported and attributed to buckling in the X-Z plane (rotation along the X-axis) [17]. Fig. 10b illustrates the side view of the component after failure. The printed part deviation (green line) from the centerline (dashed blue line) leads to in-process part failure as the laser deposits the subsequent layer on empty space. According to [17], thinner parts are more susceptible to buckling, while thicker parts are less susceptible to buckling and provide additional space for the next layer to be placed improving the LBH.

5.2.2. Failure mechanism two (incomplete top)

Failure becomes localized at the part corners, as shown in Fig. 10c. Buckling in the Y-Z plane (rotation about the Z-axis) now occurs in addition to the previously observed buckling in the X-Z plane (section 5.2.1). Fig. 10d illustrates the side view of the component after failure. The printed part deviates from the longitudinal direction (red line) and the center line (green line) due to localized deformations accumulated at the corner of the component. The LPBF process continues and deposits few more layers on a portion of the component, ultimately resulting in part failure resembling failure mechanism one. Fig. 9 shows that most short thin-wall parts exhibit type 1 failure mechanism. As the part length increases, type 2 failure mechanism becomes more dominant.

5.3. Simulation of part distortion and LBH

Part distortion and LBH are simulated using the modeling approach described in section 3. A representative subset of 6 parts built with different printing patterns and part lengths are compared with the corresponding simulations, as shown in Fig. 11. All parts are equally thick (0.5 mm), and the printing pattern and wall length are provided above each simulation figure.

The model successfully captures the general trends in part distortions for all the printing patterns and part lengths evaluated in this study. For example, the "ES-30 mm" part shown in Fig. 11a exhibits a mechanism one failure. The simulation results show excessive part displacement near the summit. This results in misplacement of the following layers with respect to the centerline (X-axis) due to buckling in the X-Z plane. Accordingly, the part tip in Fig. 11a shows material accumulation offset from the center line (see green circle). The "R-30" mm built and simulated parts (Fig. 11b) exhibit lesser distortion compared to the "ES-30 mm" part in Fig. 11a. The effect of inter-layer vector rotation on distortion is also well captured in the "R-60 mm" part in Fig. 11c. Continuous inter-layer vector rotation is well known for reducing the amount of residual stresses and distortion in LPBF parts [51]. In this study, the model predicts lower distortions when interlayer scan rotation is included (Fig. 11c) and higher distortions when no scan rotations are employed (Fig. 11d). In the latter case, both simulation and experimental part show curvature along the centerline (Z-axis) and localized distortion along the longitudinal direction (X-axis) close to the part corners. This confirms the model's capability to capture the effect of scanning strategy on part distortion.

The model can also accurately capture the effect of part length on the buckling behavior. Buckling essentially occurs along the centerline (in the X-Z plane) of the "ES-30 mm" part in Fig. 11a. Displacement is localized at the part tip and evenly distributed along the X-axis (not shown in Fig. 11a, which corresponds to type 1 failure mode. Fig. 11d and e show that increasing the part length promotes more buckling in the Y-Z plane (along the longitudinal direction) and strain localization at the part corners in both experimental (red circle regions) and simulated parts. This agrees well with the type 2 failure mode reported in Fig. 9.

The LBH is also well captured for all the conditions shown in Fig. 11,

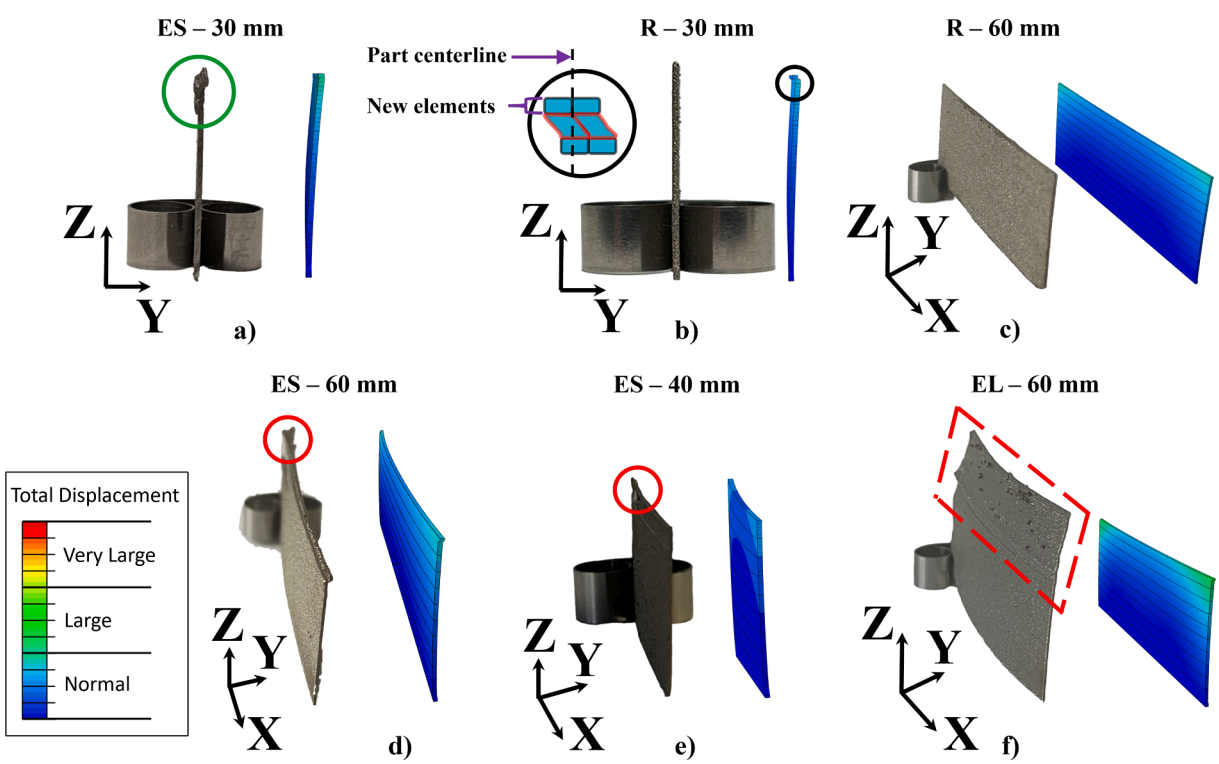

Fig. 11. Comparison between experimental (on the left) and simulated (on the right) distortion for six components with various dimensions fabricated using different printing patterns. The printing pattern and wall length are given above each figure. All thin-wall components are equally thick (0.5 mm). An example of a thin-wall part showing successful deposition of successive layers following excessive distortion is highlighted in (a) using a green circle. An example of model termination due to excessive distortion is shown in (b) using a black close-up circle. Element distortion is indicated with red outlines and the part centerline is highlighted using a black dashed line. An example of a thin-wall part showing successful deposition of successive layers following gradual distortion is highlighted in (f) using a red dashed box. (For interpretation of the references to color in this figure legend, the reader is referred to the web version of this article.)

with the exception of the longer vector length components in Fig. 11f. The effect of VL on LBH simulations is better illustrated in Fig. 12, where experimental and simulated LBH values for "ES" and "EL" printing patterns are compared. The simulation underestimates the LBH for all thin-wall part thicknesses and lengths, as shown in Fig. 12a. The simulation error is less than 10% compared to experimental results for the "ES" printing pattern in Fig. 12a. On the contrary, Fig. 12b shows a large difference (approximately 33%) between predicted and experimental LBH when longer vector length is used. These results indicate that the model fails to reproduce the impact of VL on LBH even though a directional heat source is used.

6. Discussion

The discrepancy between the model and experimental LBH is partly explained by simulation termination when results diverge due to excessive local distortion. Buckling mechanisms described in section 5.2 are significant for LBH. Buckling creates a large gap between the new layer and previously deposited layers causing the distortion of elements as highlighted using a black close-up circle in Fig. 11b. The close-up schematic shows how new elements are deposited along the centerline (black dashed line) at the part summit. Upon deposition, the new elements become displaced from the FEM elements in the previous layer, shifted off the part centerline due to buckling. In order to preserve node connectivity between the two layers, elements located at the junction (illustrated with red outlines) get distorted. The distorted elements contain large local strains exceeding the software threshold and resulting in simulation abortion.

Fig. 13 shows how stresses and strains evolve during the simulation of LPBF thin-wall parts. The simulation was taken from a 30 × 30 × 0.5 mm (length × height × thickness) part showing large variation between the experimentally observed and simulated LBH (see black columns in Fig. 12). The stress distribution in Fig. 13a remains relatively constant from the middle of the simulation (stage I) to the moment when the first sign of buckling occurs (stage III). This is because the buckling mechanism is sensitive to the part height, as discussed in [17]. Accordingly, Fig. 13b shows very little strain before the first sign of buckling (stages I and II). Only one lumped layer difference exists between stages II and III causing buckling initiation. At this moment, strain becomes localized at the top surface, and the simulation terminates rapidly following another lumped layer (stage IV) deposition because localized strain exceeds the software threshold.

A critical strain threshold does not exist in the LPBF process, and the process will continue provided the following layer can be built over a solid section, as shown using a green circle in Fig. 11a. When buckling occurs, the LPBF process continues depositing more layers and the deviation becomes larger. After a certain height, this condition creates enough deviation to suppress subsequent layer deposition. Note that the amount of strain in buckling is too high to be managed by the model solver. This causes divergence and the model aborts on the first sign of buckling. Hence, the simulation generates a conservative LBH value, where the model systematically predicts smaller LBH compared to the actual process. This is observed for the short vector length and becomes more apparent for the long vector length in Fig. 12.

The model cannot capture LBH due to the solver limitation. However, the results presented in Figs. 8 and 11 prove that the model accurately captures part distortion at different scales before part failure occurs. On the one hand, the local displacement is accurately predicted in Fig. 8 at the micro-scale. The displacement is localized along the edges in both the model and experimental 1 mm thin-wall parts. On the other hand, the model can predict different buckling mechanisms causing part bending in different planes at the macro-scale (Fig. 11).

6.1. The effect of printing pattern on residual stresses

To shed further light on the effect of vector and part lengths on the failure modes, the residual stresses are evaluated. According to [20], the maximum stress along the wall thickness (Y) is 30 and 24 times smaller than along the build direction (Z) and part length (X), respectively. This can be explained by the plane strain theory as the printed wall thickness is significantly smaller than its length and height. Therefore, only the longitudinal stress (S_{XX}) and stress in build direction (S_{ZZ}) are considered. The models are sectioned through the center to show the internal stresses.

Figs. 14 and 15 compare the residual stresses between eight different printing patterns (see Table 1) in the build (S_{ZZ}) and longitudinal (S_{XX}) directions, respectively. For a fair comparison between the printing patterns, the model dimensions are kept constant (30 mm long, 0.50 mm thick and 17 mm high). The internal stresses are mostly compressive along the build direction for all 8 printing patterns. This explains the

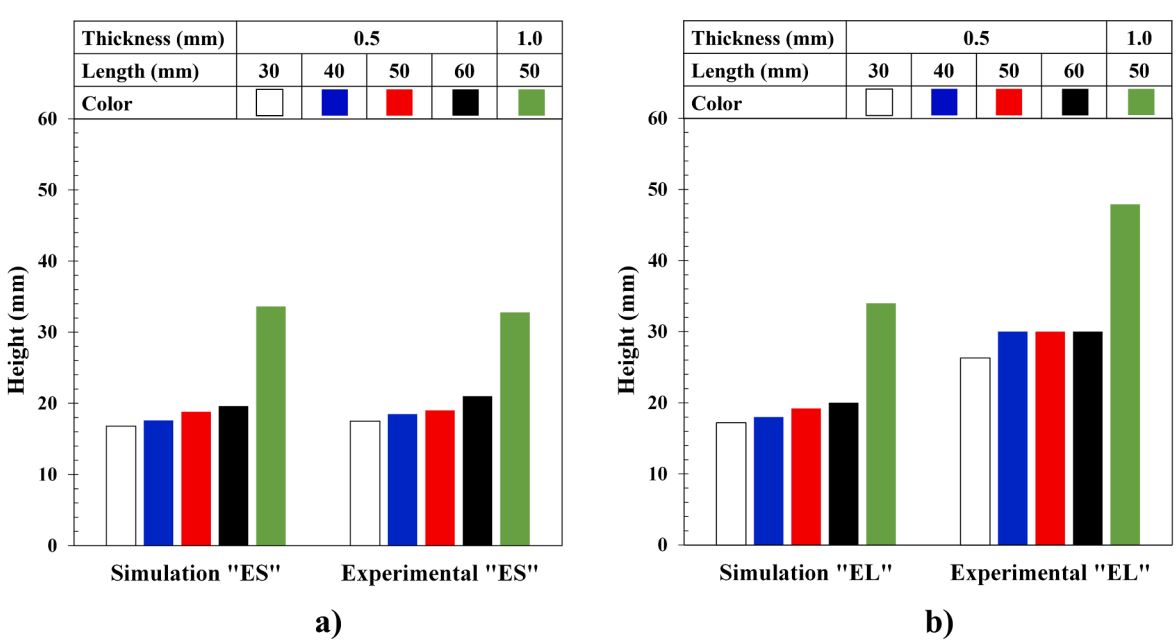

Fig. 12. Comparison between observed and simulated LBH for a) "ES" and b) "EL" printing patterns.

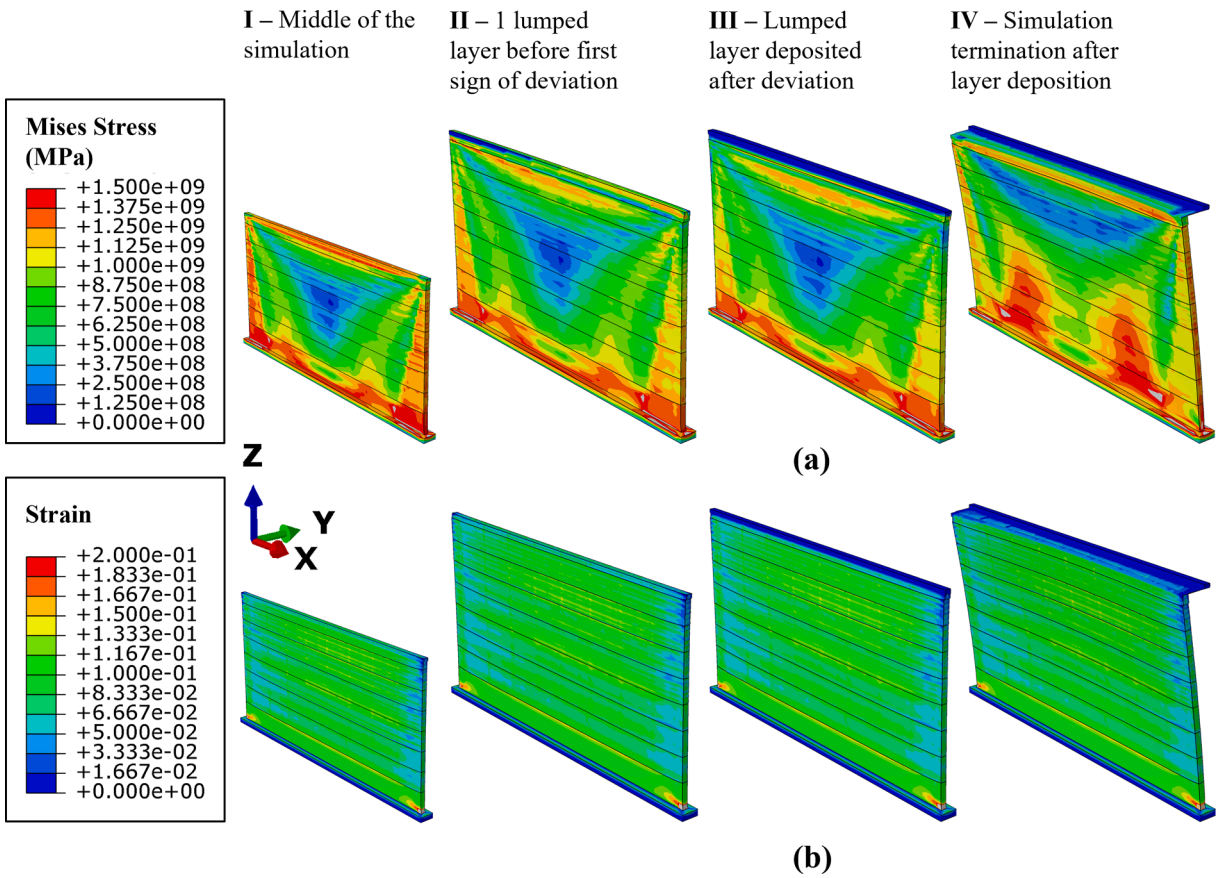

Fig. 13. FEM simulations predicting part failure due to excessive deformation during LPBF. The first and second rows illustrate (a) von Mises stress and (b) plastic strain evolution upon layer addition from the middle of the part. A thin-wall part designed to be 0.50 mm thick, 30 mm long, 30 mm tall, and processed with EL printing pattern (see Table 1) is considered.

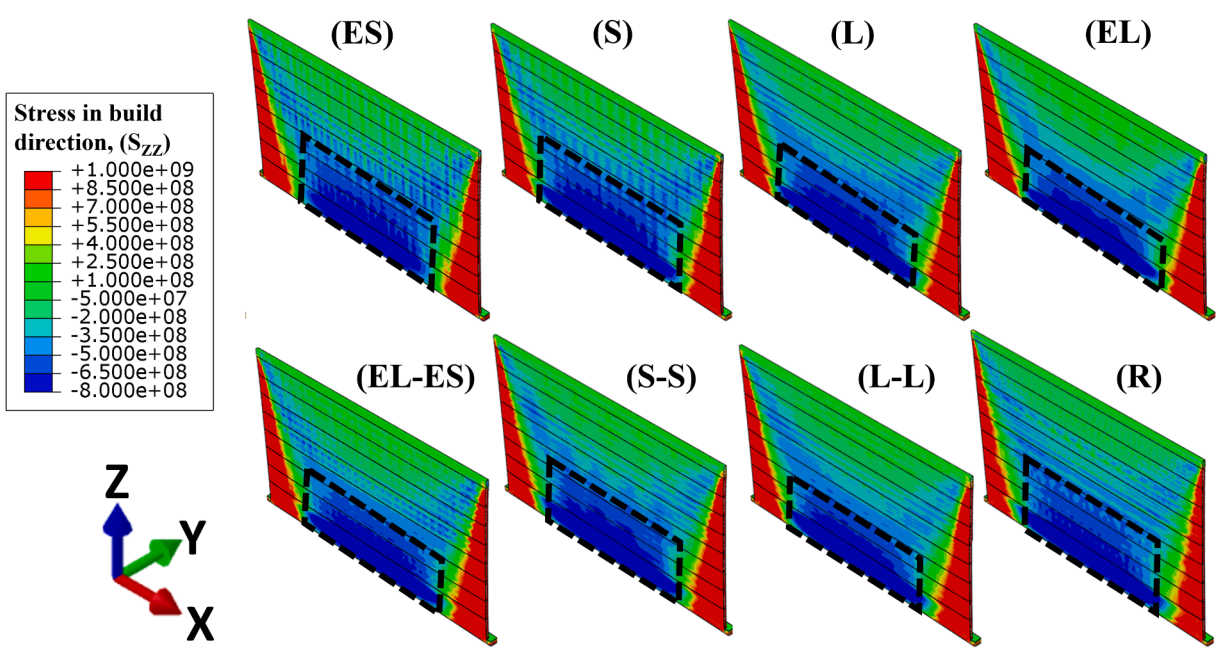

Fig. 14. Stress along the build direction (S_{ZZ}) for the 8 different printing patterns investigated. The parts' thickness, length and height are 0.50 mm, 30 mm, and 17 mm, respectively. The printing patterns are labelled on top of each component according to label descriptions in Table 1. The residual stresses are shown along a centerline cross section of the parts. Dashed black boxes are used to highlight the region exhibiting compressive stresses.

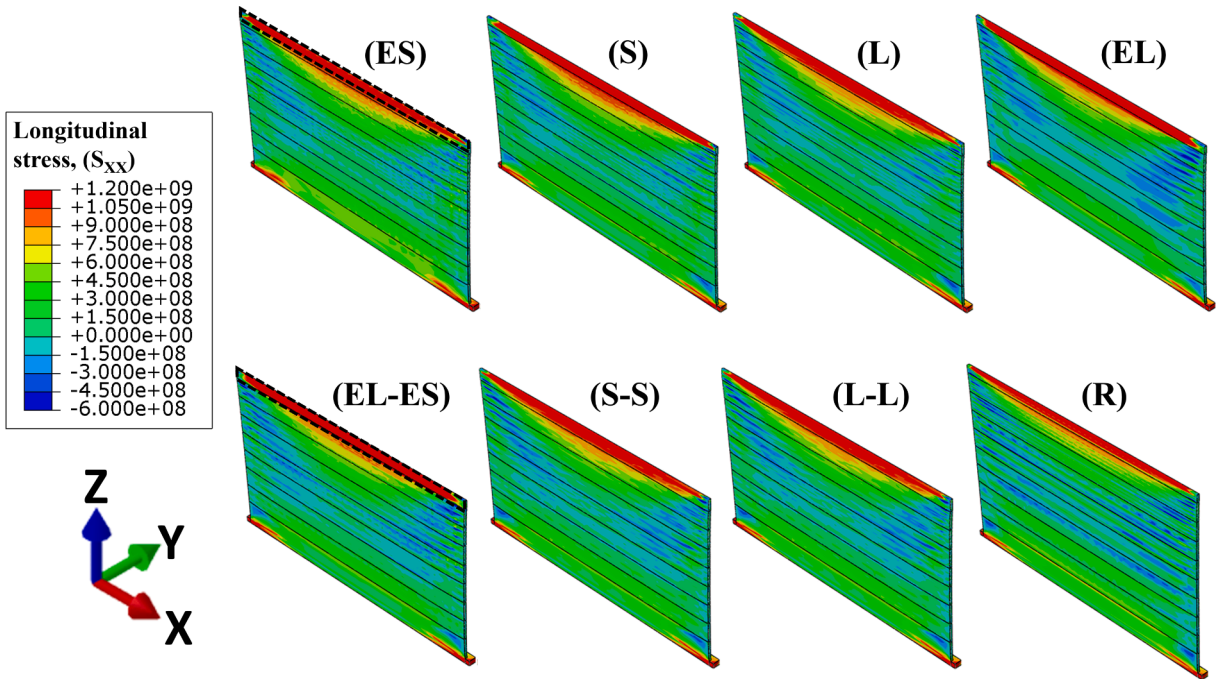

Fig. 15. Longitudinal stress (S_{XX}) for the 8 different printing patterns investigated. The common part thickness, length, and height are 0.50 mm, 30 mm, and 17 mm, respectively. The printing patterns are labelled on top of each component as shown in Table 1. The residual stresses are shown along a centerline cross section of the parts.

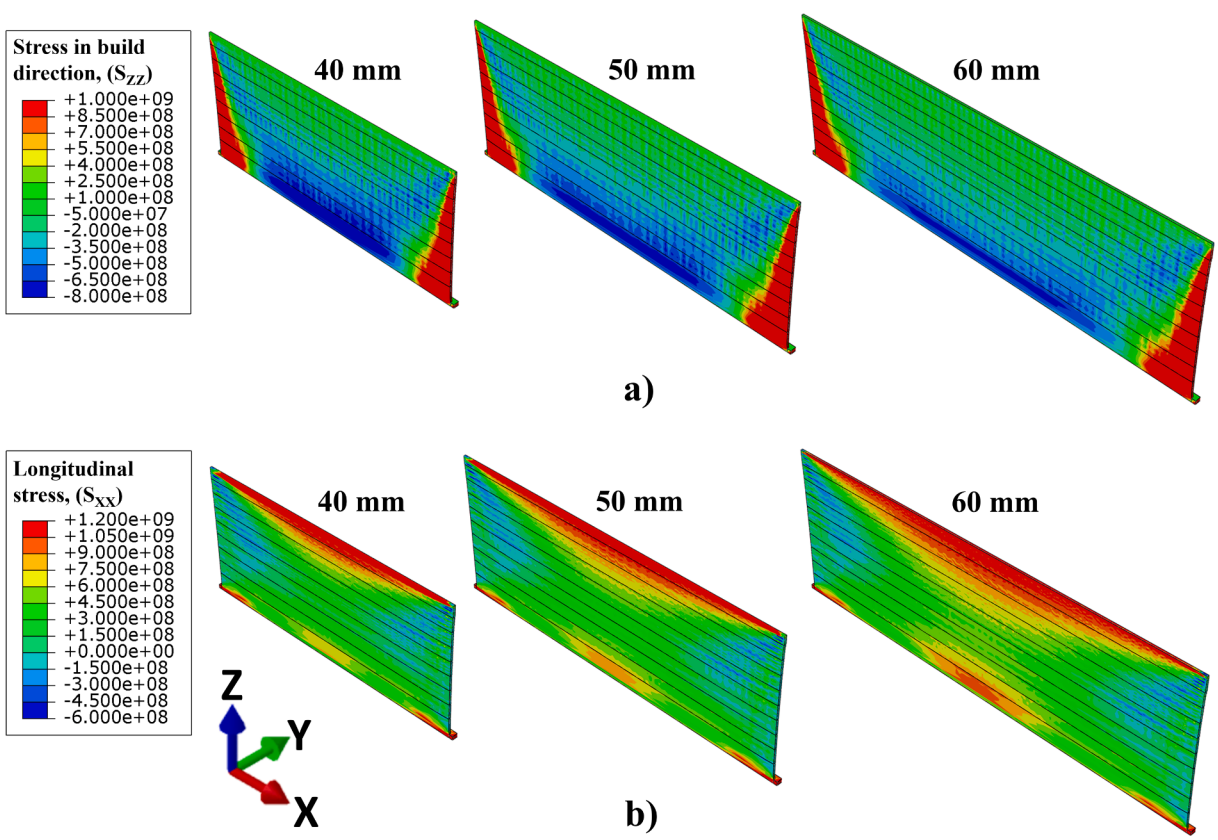

Fig. 16. Comparison between a) build direction (S_{ZZ}) and b) longitudinal (S_{XX}) residual stresses for three different part lengths. The part lengths are labelled above each component. The printing pattern is "ES", the part height is 17 mm, and the wall thickness is 0.5 mm. The residual stresses are shown along a centerline cross section of the parts.

propensity for buckling in the X-Z plane causing failure mechanisms one and two, as shown in Fig. 10. Interestingly, the compressive stress intensity regions, highlighted by the black boxes in Fig. 14, increase when the vector length decreases from "EL" to "ES". For shorter VLs, buckling is thus expected to begin at a lower height leading to a smaller LBH. Accordingly, Fig. 9a shows that the LBH decreases with the vector length. As the VL increases, compressive stresses along the BD become smaller, enabling further layer deposition before excessive buckling leads to part failure.

When a short VL is employed, the high residual stress leads to abrupt change in buckling limiting the number of subsequent layers that can be deposited. In this case, both the LBH and model predictions are similar in Fig. 12a. When the VL increases, the compressive stress along the BD decreases. This leads to less buckling and more gradual part distortion allowing more subsequent layers to be deposited. The subsequent deposited layers are highlighted by the red box in Fig. 11f. In this case, the model prediction exhibits more significant deviation compared to the experimental LBH observed in Fig. 12b.

The VL is also important when inter-layer scan rotation is introduced. Fig. 14 clearly shows how the high compressive stress intensity areas (black box) decrease when the VL increases (see difference between "S-S" and "L-L"). The "ES-EL" and "R" printing patterns produce combinations of short and long VLs causing intermediate residual compressive stress intensities. This is in good agreement with the LBH demonstrated in Fig. 9, where "S-S" and "L-L" printing patterns produce smaller and larger LBH, respectively, while "ES-EL" and "R" produce intermediate LBH values.

Fig. 15 illustrates significantly different characteristics when the stress is evaluated along the longitudinal direction (S_{XX}). The stress becomes primarily tensile with the stress concentrated at the top of the components. Interestingly, the components with longer vectors are subjected to greater compressive stresses at the top corners (see the blue regions). The EL-60 mm experimental part in Fig. 11f shows how this compressive stress promotes excessive curling in the Y-Z plane (along the longitudinal X-direction) of the corners as the bottom is constrained and the top is free to bend. This favors failure mechanism two.

6.2. The effect of part length on residual stresses

The effect of part length on the residual stresses is shown in Fig. 16. The compressive stress in the build direction (S_{zz}) causing buckling in the X-Z plane (along the centerline Z-direction) decreases significantly with part length. This is demonstrated by comparing the blue areas in the 40 mm and 60 mm long parts in Fig. 16a. This explains why failure mechanism one (excessive buckling in the X-Z plane) is less frequently observed in longer parts in Fig. 9.

Fig. 16b shows that the compressive stress magnitude along the corner in the S_{XX} direction (contributing to buckling in the Y-Z plane) remains constant with part length. According to the plate theory [52,53], buckling susceptibility in the Y-Z plane increases with the part length. Accordingly, mechanism two failure morphologies localized along the part corners are observed more frequently in longer parts in Fig. 9. In summary, as the part length increases, buckling along the Y-Z plane increases due to geometric factors and buckling in the X-Z plane decreases due to reduced compressive stresses in the build direction.

7. Conclusion

A novel framework is developed to simulate part-scale components without compromising the directionality of the stress components generated by the laser tracks. The hybrid line model, where the laser beam heat source is integrated along the track directions, is coupled with a lumping approach, which allows several laser tracks to be combined for higher computational efficiency. Furthermore, a layer lumping approach is incorporated to accelerate the simulation of low-interest component sections, and a mesh coarsening technique is used to perform nearly simultaneous thermal and mechanical simulations to minimize the computation time.

The model is used to study the distortion and underlying causes for premature part failure (LBH), frequently encountered during the LPBF of high gamma-prime Ni-based superalloy thin-wall parts. A total of 35 thin-wall components were fabricated by LPBF and compared with corresponding simulations. Eight (8) different printing patterns with different vector lengths and interlayer rotations for five (5) different part lengths were studied. The major conclusions drawn from this study are provided below:

1. Model efficiency: The directional heat source model can accurately predict the effect of scanning strategy and part dimensions on part distortion. The model can predict thin-wall part distortion accurately within 10 μm of the experimental error in reasonable time using low processing power. Each simulation only requires 12 cores of dual Intel Xeon gold 6240 processor allowing the simulation of different parts simultaneously. This makes the model especially suitable for LPBF parametric studies.

2. Simulation of LBH: The model predicts the LBH within 1.4 mm of the experimental LBH for thin-wall parts printed with short vector length scan strategies. When the vector length increases, a larger deviation (within 13.9 mm) from the observed LBH occurs due to FEM solver limitations.

3. LBH mechanism: The LBH phenomenon is shown to stem from the buckling of components during printing. The buckling modes are found to be sensitive to part dimensions, while the printing pattern influences the intensity of residual stress causing buckling.

a) A strong effect of the vector length on the LBH is observed. The LBH increases by 50%-60% with increasing VL (by decreasing scan angle).

b) Part length has smaller significance on part distortion and LBH. The part height increases only by 20% when the part length increases from 30 to 60 mm.

c) The buckling modes are found to be sensitive to part dimensions. Short part lengths exhibit mode 1 buckling with clear rupture along the part centerline aligned with BD. A shift in the buckling mode (from mode 1 to mode 2) occurs when the part length increases. Part failure becomes less homogenous and more localized along the upper part corners.

4 Residual stresses: The printing pattern and part geometry influence the intensity of residual stresses causing buckling.

a) Short vector length promotes compressive stresses along the build direction (BD) favoring buckling. Longer vector length creates less compressive stresses along BD and higher tensile stresses along the part length.

b) Interlayer vector rotation homogenizes the stress distribution within thin-wall components. This reduces the part distortion.

c) Compressive stresses along BD are concentrated at the part center when the part length is short. As the part length increases, compressive stresses become more localized at the upper part corners. This alters the buckling mechanism from mode 1 to mode 2.

d) The optimum printing conditions to maximize LBH are the ones minimizing the compressive residual stresses and part distortion. This can be achieved by maximizing the number of long vector lengths through interlayer scan rotations.

Declaration of Competing Interest

The authors declare that they have no known competing financial interests or personal relationships that could have appeared to influence the work reported in this paper.

Data availability

Data will be made available on request.

Acknowledgments

The authors are thankful to Natural Sciences and Engineering Research Council of Canada (NSERC) under Grant No. RGPIN-2019-04073. The authors would also like to thank Amber Andreaco, from GE Additive, for supplying the powder material used in this study. Étienne Martin is thankful to the Jacques L'Écuyers Industrial Research Chair Foundation.

References

[1] R.C. Reed, The superalloys: fundamentals and applications, Cambridge University Press, 2006.
[2] N. Eftekhari, W. Muhammad, F. Haftlang, A. Zarei-Hanzaki, É. Martin, Microstructural evolution and corrosion behavior of Sanicro 28 during thermomechanical processing, Mater. Today Commun. 24 (2020) 101228.
[3] J.-C. Stinville, E. Martin, M. Karadge, S. Ismonov, M. Soare, T. Hanlon, S. Sundaram, M.P. Echlin, P.G. Callahan, W.C. Lenthe, J. Miao, A.E. Wessman, R. Finlay, A. Loghin, J. Marte, T.M. Pollock, Competing modes for crack initiation from non-metallic inclusions and intrinsic microstructural features during fatigue in a polycrystalline nickel-based superalloy, Metall. Mater. Trans. A 49 (9) (2018) 3865–3873.
[4] X. Quelennec, E. Martin, L. Jiang, J.J. Jonas, Work hardening and kinetics of dynamic recrystallization in hot deformed austenite, in, J. Phys. Conf. Ser., IOP Publishing (2010) 12082.
[5] É. Martin, W. Muhammad, A.J. Detor, I. Spinelli, A. Wessman, D. Wei, "Strain-annealed" grain boundary engineering process investigated in Hastelloy-X, Materialia (Oxf). 9 (2020), 100544.
[6] W.J. Sames, F.A. List, S. Pannala, R.R. Dehoff, S.S. Babu, The metallurgy and processing science of metal additive manufacturing, Int. Mater. Rev. 61 (5) (2016) 315–360.
[7] A. Thatte, A. Loghin, E. Martin, V. Dheeradhada, Y. Shin, B. Ananthasayanam, Multi-Scale Coupled Physics Models and Experiments for Performance and Life Prediction of Supercritical CO2 Turbomachinery Components, The 5th International Symposium-Supercritical, in, 2016.
[8] M. Ziaee, N.B. Crane, Binder jetting: A review of process, materials, and methods, Addit. Manuf. 28 (2019) 781–801.
[9] E. Martin, A. Natarajan, S. Kottilingam, R. Batmaz, Binder jetting of "Hard-to-Weld" high gamma prime nickel-based superalloy RENÉ 108, Addit. Manuf. 39 (2021), 101894.
[10] W. Muhammad, R. Batmaz, A. Natarajan, E. Martin, Effect of binder jetting microstructure variability on low cycle fatigue behavior of 316L, Mater. Sci. Eng. A 839 (2022), 142820.
[11] H. Bikas, P. Stavropoulos, G. Chryssolouris, Additive manufacturing methods and modelling approaches: a critical review, Int. J. Adv. Manuf. Technol. 83 (1-4) (2016) 389–405.
[12] D. Dev Singh, T. Mahender, A. Raji Reddy, Powder bed fusion process: a brief review, Mater. Today: Proc. 46 (2021) 350–355, https://doi.org/10.1016/j.matpr.2020.08.415.
[13] A. Salmi, F. Calignano, M. Galati, E. Atzeni, An integrated design methodology for components produced by laser powder bed fusion (L-PBF) process, Virtual Phys Prototyp. 13 (2018) 191–202, https://doi.org/10.1080/17452759.2018.1442229.
[14] W.E. King, A.T. Anderson, R.M. Ferencz, N.E. Hodge, C. Kamath, S.A. Khairallah, A.M. Rubenchik, Laser powder bed fusion additive manufacturing of metals; physics, computational, and materials challenges, Appl. Phys. Rev. 2 (2015) 41304.
[15] L. Cao, J. Li, J. Hu, H. Liu, Y. Wu, Q. Zhou, Optimization of surface roughness and dimensional accuracy in LPBF additive manufacturing, Opt. Laser Technol. 142 (2021), 107246, https://doi.org/10.1016/j.optlastec.2021.107246.
[16] A. Chakraborty, R. Tangestani, W. Muhammad, T. Sabiston, J.-P. Masse, R. Batmaz, A. Wessman, É. Martin, Micro-cracking mechanism of RENÉ 108 thin-wall components built by laser powder bed fusion additive manufacturing, Mater. Today Commun. 30 (2022) 103139.
[17] A. Chakraborty, R. Tangestani, R. Batmaz, W. Muhammad, P. Plamondon, A. Wessman, L. Yuan, É. Martin, In-process failure analysis of thin-wall structures made by laser powder bed fusion additive manufacturing, J. Mater. Sci. Technol. 98 (2022) 233–243, https://doi.org/10.1016/j.jmst.2021.05.017.
[18] H.C. Taylor, E.A. Garibay, R.B. Wicker, Toward a common laser powder bed fusion qualification test artifact, Addit. Manuf. 39 (2021), 101803.
[19] S.M. Tawfik, M.N.A. Nasr, H.A. El Gamal, Finite element modelling for part distortion calculation in selective laser melting, Alex. Eng. J. 58 (1) (2019) 67–74.
[20] R. Tangestani, T. Sabiston, A. Chakraborty, L. Yuan, N. Krutz, É. Martin, An efficient track-scale model for laser powder bed fusion additive manufacturing: part 2—mechanical model, Front. Mater. 8 (2021), https://doi.org/10.3389/fmats.2021.759669.
[21] K. An, L. Yuan, L. Dial, I. Spinelli, A.D. Stoica, Y. Gao, Neutron residual stress measurement and numerical modeling in a curved thin-walled structure by laser powder bed fusion additive manufacturing, Mater. Des. 135 (2017) 122–132.
[22] M. Gouge, E. Denlinger, J. Irwin, C. Li, P. Michaleris, Experimental Validation of Thermo-mechanical Part-Scale Modeling for Laser Powder Bed Fusion Processes, Addit. Manuf. 29 (2019) 100771.
[23] B. Cheng, K. Chou, Melt pool evolution study in selective laser melting, in: 26th Annual International Solid Freeform Fabrication Symposium-An Additive Manufacturing Conference, Austin, TX, USA, 2015: pp. 1182–1194.
[24] F. Chen, W. Yan, High-fidelity modelling of thermal stress for additive manufacturing by linking thermal-fluid and mechanical models, Mater. Des. 196 (2020) 109185.
[25] D. Hu, N. Grilli, L.u. Wang, M. Yang, W. Yan, Microscale residual stresses in additively manufactured stainless steel: computational simulation, J. Mech. Phys. Solids 161 (2022) 104822.
[26] C. Li, C.H. Fu, Y.B. Guo, F.Z. Fang, A multiscale modeling approach for fast prediction of part distortion in selective laser melting, J. Mater. Process. Technol. 229 (2016) 703–712.
[27] J. Irwin, P. Michaleris, A line heat input model for additive manufacturing, J. Manuf. Sci. Eng. 138 (2016).
[28] H. Huang, Y. Wang, J. Chen, Z. Feng, A comparative study of layer heating and continuous heating methods on prediction accuracy of residual stresses in selective laser melted tube samples, Integr. Mater. Manuf. Innov. 10 (2021) 218–230, https://doi.org/10.1007/s40192-021-00217-4.
[29] M. Bayat, C.G. Klingaa, S. Mohanty, D. De Baere, J. Thorborg, N.S. Tiedje, J. H. Hattel, Part-scale thermo-mechanical modelling of distortions in Laser Powder Bed Fusion-Analysis of the sequential flash heating method with experimental validation, Addit. Manuf. 36 (2020), 101508.
[30] Z. Luo, Y. Zhao, Numerical simulation of part-level temperature fields during selective laser melting of stainless steel 316L, Int. J. Adv. Manuf. Technol. 104 (5-8) (2019) 1615–1635.
[31] Ł. Rakoczy, O. Milkovič, B. Rutkowski, R. Cygan, M. Grudzień-Rakoczy, F. Kromka, A. Zielińska-Lipiec, Characterization of γ′ precipitates in cast Ni-based superalloy and their behaviour at high-homologous temperatures studied by TEM and in Situ XRD, Materials. 13 (2020) 2397.
[32] Y. Wang, S. Roy, H. Choi, T. Rimon, Cracking suppression in additive manufacturing of hard-to-weld nickel-based superalloy through layer-wise ultrasonic impact peening, J. Manuf. Process. 80 (2022) 320–327, https://doi.org/10.1016/j.jmapro.2022.05.041.
[33] S. Catchpole-Smith, N. Aboulkhair, L. Parry, C. Tuck, I.A. Ashcroft, A. Clare, Fractal scan strategies for selective laser melting of 'unweldable'nickel superalloys, Addit. Manuf. 15 (2017) 113–122.
[34] C. Li, Z.Y. Liu, X.Y. Fang, Y.B. Guo, Residual stress in metal additive manufacturing, Procedia CIRP. 71 (2018) 348–353.
[35] Hexagon, SmartScan Data Sheet, 2022. https://hexagon.com/resources/resource-library/assets/mi/smartscan-rll25101 (accessed March 13, 2023).
[36] A.J. Torroba, O. Koeser, L. Calba, L. Maestro, E. Carreño-Morelli, M. Rahimian, S. Milenkovic, I. Sabirov, J. LLorca,, Investment casting of nozzle guide vanes from nickel-based superalloys: part I–thermal calibration and porosity prediction, Integr. Mater. Manuf. Innov. 3 (2014) 344–368.
[37] R. Przeliorz, F. Binczyk, P. Gradoń, M. Góral, T. Mikuszewski, Evaluation of heat capacity and resistance to cyclic oxidation of nickel superalloys, Arch. Foundry Eng. 14 (3) (2014) 67–70.
[38] C. Li, M.F. Gouge, E.R. Denlinger, J.E. Irwin, P. Michaleris, Estimation of part-to-powder heat losses as surface convection in laser powder bed fusion, Addit. Manuf. 26 (2019) 258–269.
[39] T.P. Gabb, J. Gayda, P.T. Kantzos, T. Biles, W. Konkel, The tensile properties of advanced nickel-base disk superalloys during quenching heat treatments, in: 2001 Fall Meeting, 2001.
[40] J.C. Simo, T.J.R. Hughes, Computational inelasticity, Springer Science & Business Media, 2006.
[41] M. Mostafaei, S.M. Abbasi, Solutioning and solidification process control in Ta-modified CM247 LC superalloy, J. Mater. Process. Technol. 231 (2016) 113–124.
[42] R. Pramod, S. Mohan Kumar, A. Rajesh Kannan, N. Siva Shanmugam, R. Tangestani, Fabrication of gas metal arc welding based wire plus arc additive manufactured 347 stainless steel structure: behavioral analysis through experimentation and finite element method, Met. Mater. Int. 28 (2022) 307–321.
[43] L.-E. Lindgren, A. Lundbäck, M. Fisk, R. Pederson, J. Andersson, Simulation of additive manufacturing using coupled constitutive and microstructure models, Addit. Manuf. 12 (2016) 144–158.
[44] R. Tangestani, T.D. Sabiston, A. Chakraborty, W. Muhammad, L. YUAN, É. Martin,, An efficient track-scale model for laser powder bed fusion additive manufacturing: Part 1-thermal model, Front. Mater. (2021) 477.
[45] J. Thorborg, P. Esser, M. Bayat, Thermomechanical modeling of additively manufactured structural parts - different approaches on the macroscale, IOP Conf. Ser. Mater. Sci. Eng. 861 (2020) 12008, https://doi.org/10.1088/1757-899x/861/1/012008.
[46] M. Bugatti, Q. Semeraro, Limitations of the inherent strain method in simulating powder bed fusion processes, Addit. Manuf. 23 (2018) 329–346.
[47] T.Q. Phan, M. Strantza, M.R. Hill, T.H. Gnaupel-Herold, J. Heigel, C.R. D'Elia, A. T. DeWald, B. Clausen, D.C. Pagan, J.Y. Peter Ko, D.W. Brown, L.E. Levine, Elastic residual strain and stress measurements and corresponding part deflections of 3D additive manufacturing builds of IN625 AM-bench artifacts using neutron diffraction, synchrotron X-ray diffraction, and contour method, Integr. Mater. Manuf. Innov. 8 (3) (2019) 318–334.
[48] S. Jayanath, A. Achuthan, A computationally efficient finite element framework to simulate additive manufacturing processes, J. Manuf. Sci. Eng. 140 (2018) 41009.
[49] F. Hajializadeh, A. Ince, Finite element–based numerical modeling framework for additive manufacturing process, Material Design & Processing Communications. 1 (1) (2019) e28.
[50] E.M.R. Tangestani, A. Chakraborty, T. Sabiston, Interdependent influences of the laser power and printing pattern on residual stresses in laser powder bed fusion

additive manufacturing, in: in: Proceedings M2D2022 - 9th international Conference on Mechanics and Materials in Design, 2022, pp. 879–884.
[51] J.H. Robinson, I.R.T. Ashton, E. Jones, P. Fox, C. Sutcliffe, The effect of hatch angle rotation on parts manufactured using selective laser melting, Rapid Prototyp. J. 25 (2) (2019) 289–298.
[52] D.W.A. Rees, Mechanics of optimal structural design: minimum weight structures, John Wiley & Sons, 2009.
[53] A.C. Ugural, Stresses in beams, plates, and shells, CRC Press, 2009.